PAPER

Effect of porosity and active area on the assessment of catalytic activity of non-precious metal electrocatalyst for oxygen reduction

IOP Publishing Journal of Physics: Condensed Matter
J. Phys.: Condens. Matter **33** (2021) 324001 (12pp) https://doi.org/10.1088/1361-648X/ac0382

Effect of porosity and active area on the assessment of catalytic activity of non-precious metal electrocatalyst for oxygen reduction

Federico Gabriel Davia[1], Cynthia Carolina Fernández[1,2], Federico José Williams[1,2] and Ernesto Julio Calvo[1,2,*]

[1] Instituto de Química Física de los Materiales, Medio Ambiente y Energía INQUIMAE, CONICET, Universidad de Buenos Aires, Buenos Aires, Argentina
[2] Departamento de Química Inorgánica, Analítica y Química Física, Facultad de Ciencias Exactas y Naturales, Universidad de Buenos Aires, Buenos Aires, Argentina

E-mail: ernestojulio.calvo@gmail.com

Received 31 March 2021, revised 9 May 2021
Accepted for publication 20 May 2021
Published 22 June 2021

Abstract

We describe a method to study porous thin-films deposited onto rotating disc electrodes (RDE) applied to non-platinum group electrocatalyst obtained by pyrolysis of iron phthalocyanine and carbon, FePc/C. The electroactive area and porous properties of the thin film electrodes were obtained using electrochemical impedance spectroscopy under the framework of de Levie impedance model. The electrocatalytic activity of different electrodes was correlated to the total electroactive area (A_p) and the penetration ratio parameter through the film under ac current. The cylindrical pore model was extended to the RDE boundary conditions and derived in a Koutecky–Levich type expression that allowed to separate the effect of the electroactive area and structural properties. The resulting specific electrocatalytic activity of FePc/C heat treated at different temperatures was correlated to FePc surface concentration.

Keywords: porosity, electrocatalysis, oxygen reduction reaction, rotating disc electrode, diffusion penetration depth, x-ray photoelectron spectroscopy

(Some figures may appear in colour only in the online journal)

1. Introduction

Polymer electrolyte fuel cells are a promising technology to replace fossil fuels in the development of the 'hydrogen economy' [1]. One of the mayor challenges relies in obtaining low cost, high activity and durable electrocatalyst for the oxygen reduction reaction (ORR). The best results were obtained with platinum nanoparticles deposited onto high surface area carbon blacks, but the scarcity of the metal motivated to look for alternatives composed exclusively by abundant elements [2, 3]. Several groups [3–16] have shown that functionalized carbons obtained by pyrolysis of nitrogen and abundant transition metal precursors have activities comparable to Pt-based catalyst both in alkaline and acid media and reduces oxygen mostly to water (four electron process). Further optimization of these materials could lead to a replacement of Pt-based catalyst and can be achieved by having a better understanding of the nature of the active sites [11, 17–22].

Electrocatalyst powders are synthetized, characterized and their activity assessed with an electrochemical half-cell technique such as rotating disk electrode (RDE). RDE is an hydrodynamic electrochemical technique whose strength relies on the mathematical description of the velocity profile of the fluid near the rotating working electrode given by von

* Author to whom any correspondence should be addressed.

Karman [23] and, consequently, the analytical convective diffusion Koutecky–Levich equation [24]. The electro-catalysts are commonly deposited onto the disc (working electrode) as a porous thin-film where, ideally, all particles are electrically connected and homogeneously distributed. Special care in preparation conditions must be taken as they greatly affect the deposited film quality and, therefore, the electrocatalytic activity [25–27].

It is known that the structural properties of porous electrodes strongly affects their polarization characteristics [28, 29]. Gonzalez *et al* reported studies of the ORR on Pt/C rotating disk electrodes with thin porous coating in alkaline solutions in the framework of a thin-film/flooded-agglomerate model of gas diffusion electrodes [30].

Since electrocatalytic activity depends on the surface chemical composition, specific area and structural properties of the electrode, it is difficult to compare activities of electrodes with different surface chemical composition if the analysis does not consider the effect of last two. Herein we present a method based on rotating disk electrode and electrochemical impedance measurements to separate the effect on the activity of the specific area and structural properties. The relation between the porous thin-film properties and their catalytic activity determined by RDE was studied using a non-platinum group catalyst obtained by pyrolysis of iron phthalocyanine deposited onto Vulcan^{TM} (Cabot corp.) carbon. Porous electrode properties were obtained using impedance electrochemical analysis under the framework of the de Levie's [31] impedance model. The catalytic activity of different electrodes was correlated to the total electroactive area (A_p) and the penetration ratio parameter under alternating current flow through the film. By extending cylindrical pore model description used by de Levie to the RDE boundary conditions, an expression analogous to Koutecky–Levich equation was derived and allowed to normalize the kinetic current so it scales per unit of electroactive area. Finally, the trend observed in the specific electrocatalytic activity was explained by combination of x-ray photoelectron spectroscopy (XPS) with cyclic voltammetry experimental results.

2. Materials and methods

Vulcan^{TM} carbon was purchased from Cabot Int., cleaned with 15% hydrochloric acid to remove surface impurities and washed with milliQ^{TM} water. Iron(II) phthalocyanine, 11-mercapto-1-unde-canol and KOH were purchased from Sigma Aldrich and used without further purification.

Vulcan^{TM} carbon (200 mg) was dispersed in acetone (100 ml), FePc (80 mg) was added after deoxygenating by bubbling argon (99.9%) for 20 min and the mixture was stirred for 2 h. Then, it was added to cold milliQ^{TM} water dropwise to force FePc precipitation onto the particles, filtered, washed with cold milliQ^{TM} water and vacuum dried at 80 °C. Fractions of the resulting material were heat treated into a tubular furnace in argon atmosphere at 300 °C, 600 °C and 800 °C respectively for 2 h (with a temperature ramp of 10 °C min^{-1}).

XPS measurements were conducted in an ultrahigh vacuum chamber with a base pressure below 5×10^{-10} mbar, using a 150 mm hemispherical SPECS electron energy analyzer and an Mg Kα x-ray source. The reported binding energies were referenced to the Au 4f7/2 signal of Au(111) at 84 eV. N 1s and Fe 2p atomic ratios were calculated from the integrated intensities of core levels after instrumental and photoionization cross-section corrections.

The electrochemical experiments were performed with an Autolab V 30 (Eco Chemie, Utrecht, The Netherlands) controlled using the NOVA 2.0 software. All electrochemical experiments were carried out at room temperature in a three-electrode glass cell. A Pt counter electrode and an Ag/AgCl (3 M KCl) reference electrode were employed. Potentials herein are reported with respect to reversible hydrogen electrode (RHE). All experiments were carried using freshly prepared KOH 0.1 M solutions (pH = 13). Cyclic voltammograms were performed at 0.1 V s^{-1} under argon (99.9%) saturated solution after bubbling for 25 min and leaving an argon blanket above the solution. In all cases 50 cycles were performed. Electrochemical impedance spectroscopy was carried out at 1 V (vs RHE) after cyclic voltammetry and repeated after ORR testing, always under argon saturated solutions. A full spectrum of frequencies between 0.1 Hz and 100 kHz was applied while recording the phase angle (ø), and both real (Z') and imaginary (Z'') components of the impedance with a 10 mV peak to peak sinusoidal input signal. For RDE measurements a rotating gold-disk (0.196 cm^2) electrode was employed in an O_2 (99.9%) saturated solution at a scan rate of 2 mV s^{-1} and rotating frequency of 4 Hz.

The catalysts were tested by preparing a slurry of carbon particles covered with the catalyst and depositing onto the Au-disk electrode. First, the Au electrode was polished with 3M®1200 grit emery paper followed by: (i) 5, 1, 0.3 and 0.05 μm alumina (Buehler) each followed by 5 min sonication in isopropanol-water solution to remove excess alumina. Then, electrochemical cleaning was carried by cycling the working electrode potential from 0.4 V to 1.5 V (vs Ag/AgCl) in an argon saturated 0.5 M $HClO_4$ aqueous solution until the typical cyclic voltammetry of clean gold was obtained. The electrodes were incubated for 2 h in a 5 mM ethanol solution of 11-mercapto-1-undecanol and then washed with ethanol and Milli-Q water to form a self-assembled monolayer that blocks ORR on the thiol covered gold surface. It was verified that the self-assembled thiol was stable under the experimental conditions and that it did not affect catalyst performance, allowing electron transfer from the gold to the C/catalyst particles. The ink was prepared by dispersing 5 mg of the catalyst in 500 μl of isopropanol using NAFION® as a binder (0.5 mg). A $\sim$ 30 μg thin film was deposited onto the Au-electrode by dropping 3 μl of the ink and allow drying.

3. Results and discussion

Scheme 1 depicts schematically the preparation of the catalytic materials. The electro catalysts were tested in a three-electrode cell using a RDE. Figure 1 shows the RDE currents obtained in O_2 saturated 0.1 M KOH (pH = 13) for two electrodes

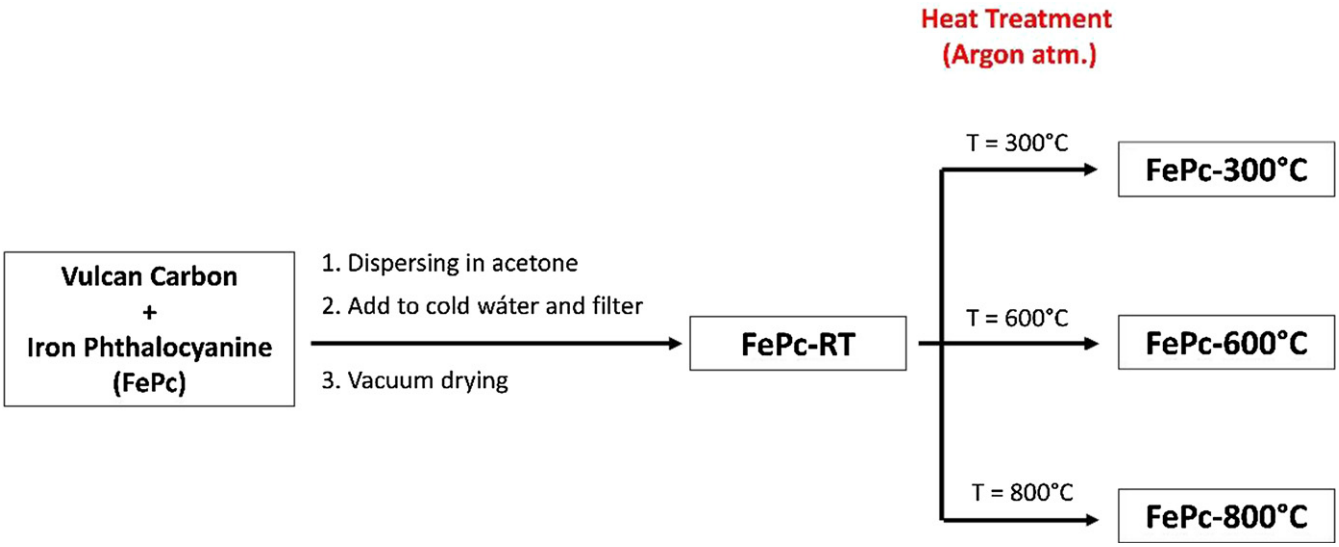

Scheme 1. Catalyst preparation process.

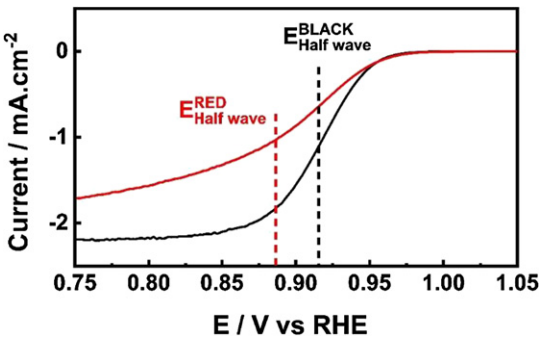

Figure 1. RDE linear scan voltammetry of two electrodes prepared from the same ink at room temperature (not heat-treated material).

prepared with the same FePc-RT ink, but different porous structure. Both curves show similar onset-potential but a clear difference can be seen at more reducing potentials, which highlights the need to define a criterion to assess the electrocatalytic activity. The onset potential as a criterion has the advantage of not being affected by the convective–diffusion contribution, but its definition is ambiguous to assess the specific electro catalytic activity [25]. On the other hand, it is worth comparing the electrocatalyst activity at higher current density under conditions close to fuel cell operation, i.e. at a potential where the current is half of the limiting current ($E_{\text{Half wave}}$) may be a better criterion. It should be emphasized that the same catalyst may show different half wave potentials even for the same preparation procedure because of differences in the porous structure of the films and electroactive sites or difference in the velocity profiles induced by the not flat thin film electrode.

The porous properties of thin films containing electrocatalyst can be assessed by the impedance response at potentials where no faradaic process takes place. The two most popular impedance models for porous electrodes are the cylindrical pore model, first introduced by de Levie [32], and the macrohomogeneous model given by Newman [33, 34]. We have used de Levie's model since it offers a simpler description. Equation (1) gives the impedance of a pore:

$$Z_{\text{p}} = \frac{l}{\rho \cdot \pi \cdot r^2} \cdot \left(\frac{1}{2} \sqrt{\frac{r}{\rho C_{\text{dl}} \omega^{\theta} l^2}} \cdot \sqrt{\frac{2}{j}} \right) \cdot \coth \left(\left(\frac{1}{2} \sqrt{\frac{r}{\rho C_{\text{dl}} \omega^{\theta} l^2}} \cdot \sqrt{\frac{2}{j}} \right)^{-1} \right). \quad (1)$$

Where l is the average length of the pore, r is the radio of the pore, ρ is the resistivity of electrolyte (Ohm.cm), ω is the frequency of the alternating current (rad.Hz), C_{dl} is the specific double layer capacity (F cm^{-2}) and θ is the constant phase element exponent.

As shown by Lasia [35] and Song *et al* [36], the impedance can be expressed in terms of the pore area and the penetration ratio of the alternating current through the pore. The area of the pore is $A_{\text{p}} = 2\pi rl$, and the penetration ratio is defined as $\alpha = \frac{1}{2}\sqrt{\frac{r}{\rho C_{\text{dl}} \omega^{\theta} l^2}}$ ($\alpha = \frac{\lambda}{l}$). By replacing in equation (1), we get:

$$Z_{\text{p}} = \left(\frac{1}{A_{\text{p}} \cdot 2 \cdot C_{\text{dl}} \omega^{\theta}} \right) \frac{1}{\alpha} \sqrt{\frac{2}{j}} \coth \left(\left(\alpha \cdot \sqrt{\frac{2}{j}} \right)^{-1} \right). \quad (2)$$

We can write the penetration ratio as $\alpha = \alpha_0 \cdot \omega^{-\frac{\theta}{2}}$, where α_0 is the penetrability coefficient. Also, we express admittances instead of impedances since the electrode have many pores and the total admittance is equal to the sum of the admittances of all pores in parallel (equation (3)).

$$Y_{\text{total}} = \left(C_{\text{dl}} \omega^{\theta} \right) \sum_{i=1}^{n} A_{\text{p},i} \frac{\tanh \left(\frac{\omega^{\frac{\theta}{2}}}{\alpha_{0,i}} \cdot \sqrt{\frac{j}{2}} \right)}{\frac{\omega^{\frac{\theta}{2}}}{\alpha_{0,i}} \cdot \sqrt{\frac{j}{2}}} j. \quad (3)$$

Note that the total admittance is the module of the admittance of a flat electrode $\left(C_{\text{dl}} \omega^{\theta} \right)$ multiplied by a factor that depends

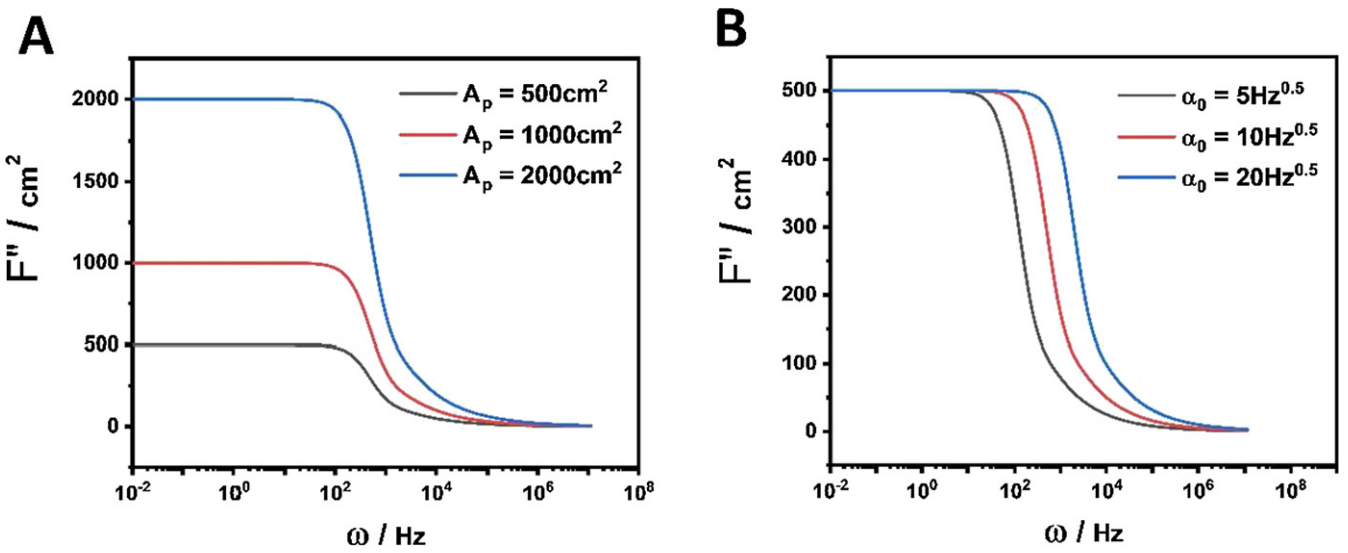

Figure 2. Simulations of $F''_{(\omega)}$. It was assumed all pores having the same α_0 and $\theta = 1$. (A) Effect of total electroactive area ($\alpha_0 = 10$ Hz$^{0.5}$). (B) Effect of α_0 ($A_p = 500$ cm^2).

on the penetration ratio and the total area of the pores. This modulating factor is a function of a complex dimensionless variable, $\frac{\omega^{\frac{\theta}{2}}}{\alpha_{0,i}}\sqrt{\frac{j}{2}}$, and is maximum at low frequencies, when the dimensionless variable is close to 0 and the hyperbolic tangent can be approximated to its argument. In this case, the total admittance equals the product of the specific admittance of a flat electrode and the total electroactive area A_p (see equation (4)) and corresponds to the case when the alternating current wave penetrates throughout all the pores.

$$Y_{\text{total}}|_{\text{low frequencies}} = \left(C_{\text{dl}}\omega^{\theta}\sum_{i=1}^{n}A_{p,i}\right)j = C_{\text{dl}}\omega^{\theta}A_p j. \quad (4)$$

We decided to use the imaginary part of the modulating factor (equation (5)) to analyze the electrodes since it is easier to interpret and contains all the information on porous properties that can be obtained from EIS analysis.

$$F''_{(\omega)} = \frac{Y''_{\text{Total}}}{C_{\text{dl}}\omega^{\theta}} = \sum_i A_{p_i}\cdot X_{i_{(\omega)}}. \quad (5)$$

Where,

$$X_{i_{(\omega)}} = \frac{\text{sen}\left(\frac{\omega^{\frac{\theta}{2}}}{\alpha_{0,i}}\right) + \text{senh}\left(\frac{\omega^{\frac{\theta}{2}}}{\alpha_{0,i}}\right)}{\frac{\omega^{\frac{\theta}{2}}}{\alpha_{0,i}}\left(\cos\left(\frac{\omega^{\frac{\theta}{2}}}{\alpha_{0,i}}\right) + \cosh\left(\frac{\omega^{\frac{\theta}{2}}}{\alpha_{0,i}}\right)\right)}. \quad (6)$$

Simulations of $F''_{(\omega)}$ depicted in figure 2 show that the curves have a sigmoidal shape. The plateau observed at low frequencies reflects the total electroactive area, as discussed above (equation (4)). At frequencies close to ${\alpha_{0,i}}^2$, the hyperbolic tangent tends to 1 and the modulating factor decreases. Electrodes with larger α_0 are comprised by wider, shorter and/or more conductive pores through which alternating current can penetrate easier, and will have associated F'' decreasing at higher frequencies.

Figure 3(A) shows the Nyquist plots of the same electrodes shown in figure 1 (colors match), and figure 3(B) shows the imaginary part of the modulating factor ($F''_{(\omega)}$). The plateau observed in the curves depicted in figure 3(B) corresponds to the low frequency limit discussed above and indicates that the electrode that corresponds to the red curve has more electroactive area per unit of geometric area than the black one. On the other hand, the red curve has a smaller α_0 since the inflection point of the curve appears at lower frequencies. $F''_{(\omega)}$ was fitted with a linear combination of $X_{i_{(\omega)}}$ (see equation (5)) obtained by using a set of 20 logarithmically equidistant $\alpha_{0,i}$ between 10^{-2} Hz$^{0.5}$ and 10^4 Hz$^{0.5}$. The obtained coefficients A_{p_i} correspond to the electroactive area of the pores with a penetration factor $\alpha_{0,i}$, and are shown in figure 3(C) (normalized by the total electroactive area of each electrode). The distribution corresponding to the red curve electrode is centered at lower values indicating that the porous film on the electrode corresponding to the red curve has thinner, longer and less conductive pores, as depicted pictorially in figure 3(D), in which the alternating current has shorter penetration.

Once the method to characterize thin porous RDE electrodes was validated, different thin film electrodes were prepared with the FePc-RT, FePC-300 °C, FePc-600 °C and FePc-800 °C catalysts which were characterized by impedance spectroscopy (EIS) at potentials where no Faradic processes takes place. The total electroactive area, A_p, and the α_0 distributions of each electrode were determined following the procedure described above. Figure 4 shows the two parameters used to describe porous properties for the different electrodes, i.e. the weighted average of α_0 (top panel) and the total electroactive area per unit of geometric area (bottom panel). EIS analysis was performed before and after determination of ORR activity and in all cases differences less than 2% in $\overline{\alpha_0}$ and A_p were obtained so that the dispersion observed was not due to experimental error but to differences in porous thin films properties in spite of the same preparation procedure.

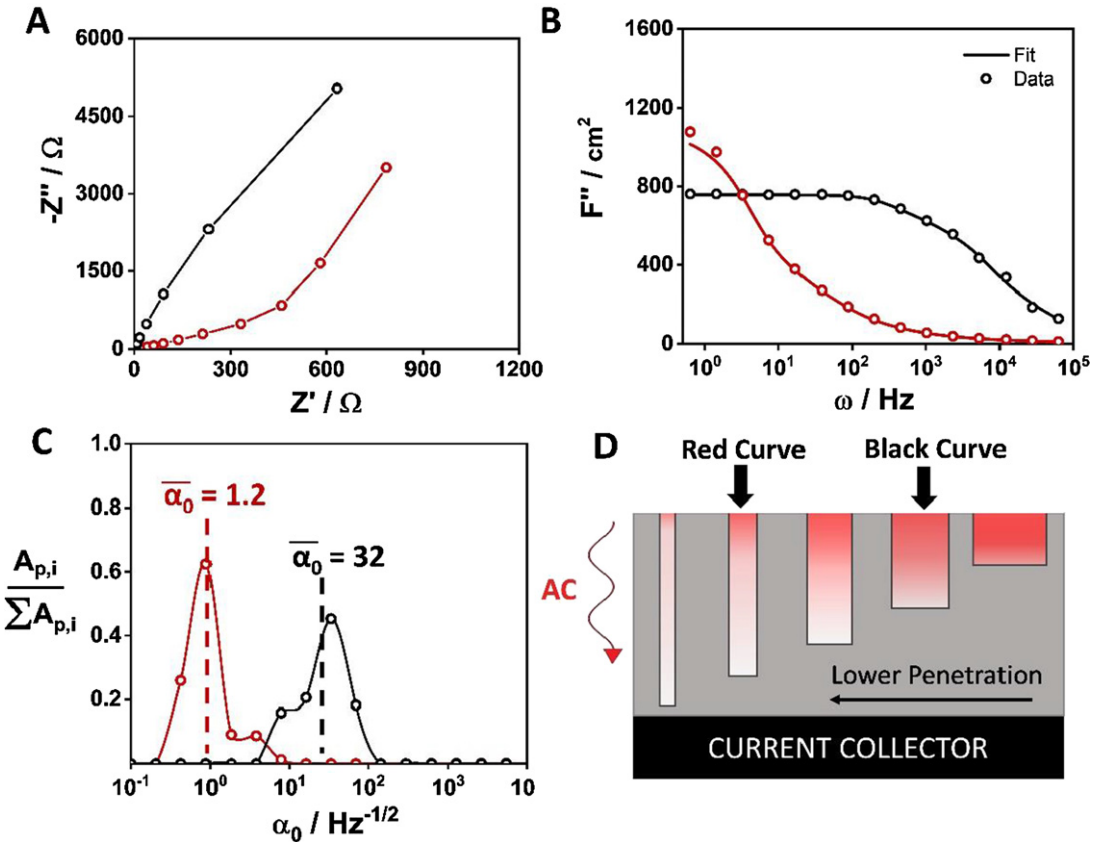

Figure 3. Impedance response of the same electrodes shown in figure 1 (colors match). (A) Nyquist plots. (B) Imaginary admittance divided by the admittance of a flat electrode as a function of the frequency. The admittances were calculated after subtracting the electrolyte resistance contribution. The exponential coefficient in the admittance of the flat electrode was obtained from the plots with values between 0.955 and 0.965. A specific capacity of 2 μF cm^{-2} was assumed. (C) Distribution of A_p as function of α_0 obtained by fitting the experimental data to equation (5). (D) Pictorial description of porous electrodes. The red curve corresponds to thinner, longer and/or less conductive pores, in which alternating current has lower penetration.

The bottom panel in figure 4 indicates that heat treatment modifies the specific electroactive area of the electrode materials. Since activity in Fe–N–C catalyst depends on the electrode porous surface area [37, 38], activity must be normalized in order to determine the influence of the surface chemical composition.

Electrocatalytic activity for the ORR was assessed by the Koutecky–Levich kinetic current (see equation (7)) to offset the diffusion–convective contribution.

$$i_k = \frac{i \cdot i_{\text{lim}}}{i_{\text{lim}} - i}. \tag{7}$$

Figure 5 shows the kinetic current obtained for three electrodes prepared using the same FePc-RT ink. At low electrode potentials, when the current approaches the limiting current, small differences in the denominator result in large noise in i_k. The noise is higher for the black and blue curves because at those potentials the current in both electrodes is very close to the limiting current.

Since all electrodes were prepared using the same catalyst and preparation procedure, one would expect overlapping curves. However, at both low and high overpotential (HO) a high dispersion was observed. On the other hand, the Tafel slopes change from −110 mV to −30 mV between 0.9 mV

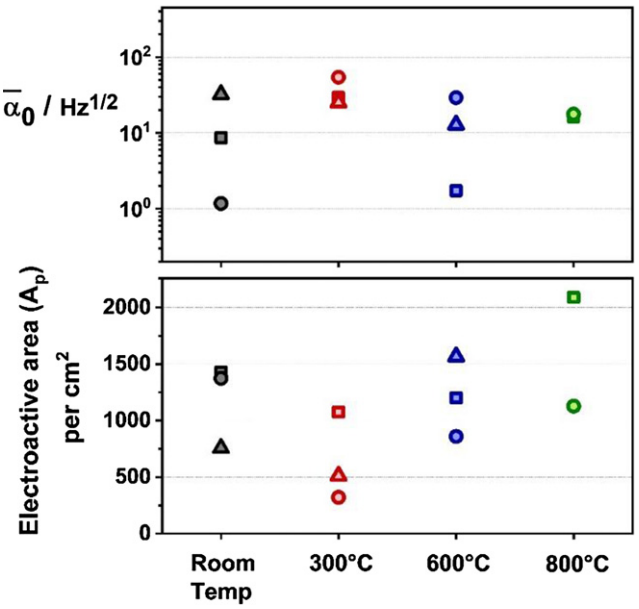

Figure 4. Results of impedance characterization of electrodes. To panel: average α_0. Bottom panel: electroactive area per unit of geometric area. Symbols refer to the number of the electrode: square correspond to the first electrode prepared, the circle to the second and the triangle to the third one.

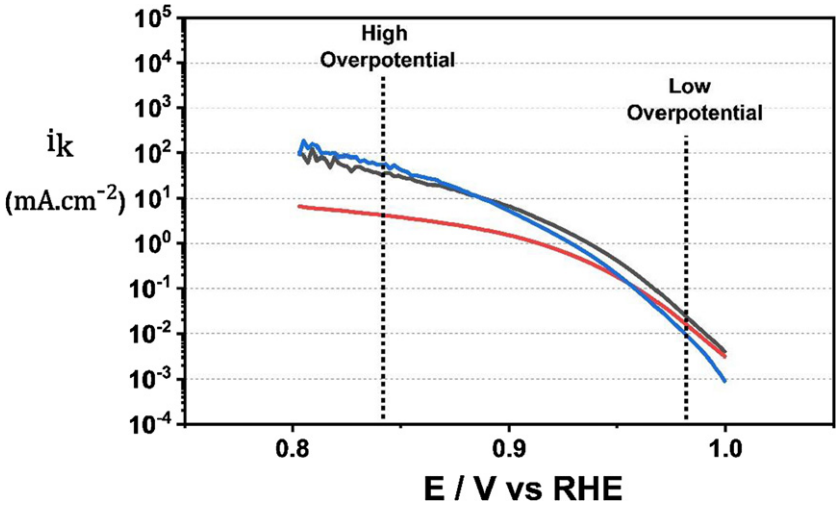

Figure 5. Kinetic current obtained for three electrodes prepared using the same FePc-RT ink. Dotted lines shows the potentials chosen for comparing the activities of the electrodes at high and low overpotential.

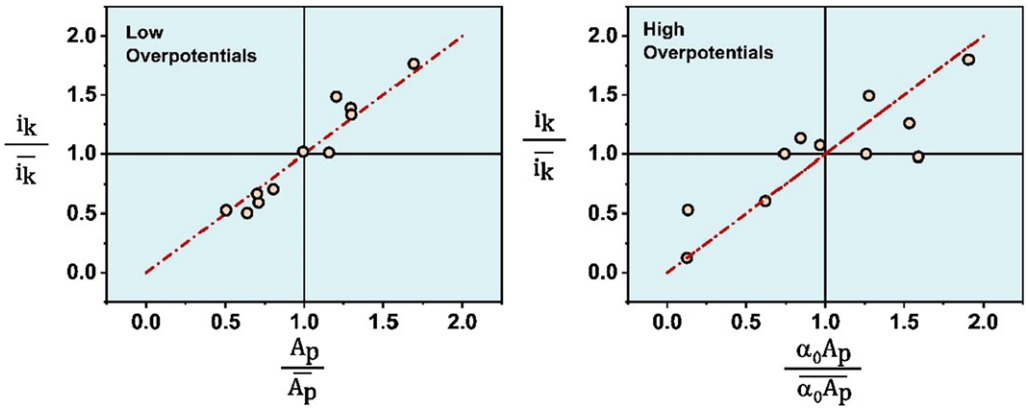

Figure 6. Deviation of i_k at low and HO (relative to the average value of each material) and the corresponding deviation of A_p and the product $\overline{A_\mathrm{p}\alpha_0}$.

and 0.95 mV, which has been ascribed to a change in ORR mechanism.

The dispersion observed in figure 5 was apparent for the other catalysts and suggests the need for a proper normalization of the electro catalytic activity. In our hands the dispersion is associated to the porous structure of the film electrode and changes in the fluid velocity profiles. Figure 6(A) shows a correlation between the deviation of i_k relative to the average value of each catalyst and the corresponding deviation of A_p at low overpotential. This suggests that the main cause of dispersion is the total electroactive area. Also, figure 6(B) shows a correlation of $i_k/\overline{i_k}$ at HO with the corresponding deviation of the product $\overline{A_\mathrm{p}\alpha_0}$. This suggests that electrodes porous properties also affect currents at higher overpotential.

Using the cylinder pore model described by de Levie for the impedance data, we derived an analogous expression for the porous thin film RDE experiments. We assumed that the film was thin enough not to affect the velocity profile of the fluid which is valid at low rotation frequency, i.e. the convective–diffusion layer thickness is much larger than the thickness of the porous thin film on the RDE. Convection is neglected inside the pores, and an O_2 consuming factor describes the oxygen depletion under first order ORR. The consuming factor is proportional to the O_2 concentration, the kinetic constant and the electrode surface area (see equation (6)), as described in the work of Lasia [35]. A pictorial description of a pore used to derive the model is shown in scheme 2.

Following the work of Lasia [35] the differential equation that describes diffusion inside the porous electrodes is:

$$\frac{\partial^2 a}{\partial z^2}(z) = \kappa^2 a(z) \tag{8}$$

with the normalized concentration inside the pore, $a(z) = C(z)/C^*$, the normalized distance $z = x/l$ and $\kappa = \frac{2\cdot k\cdot l^2}{D\cdot r}$. Considering zero O_2 flux at the bottom of the pore $\left(\frac{\mathrm{dc}}{\mathrm{dz}}\big|_{z=-l} = 0\right)$ integration yields the relationship between the normalized concentration and the relative position to be:

$$a(z) = C_0 \cdot \frac{\cosh(\kappa\cdot(z+1))}{\cosh(\kappa)}. \tag{9}$$

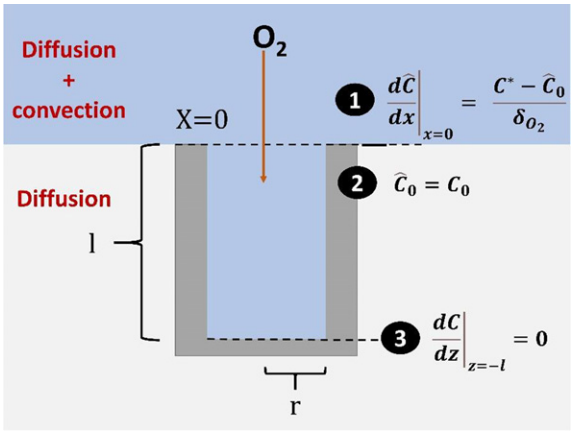

Scheme 2. Pictorial representation of a pore. The parameters used to describe it where its length 'l' and radius 'r'. Inside the pore convection was neglected.

Where C_0 is the O_2 concentration at $x = 0$. Then, the O_2 concentration gradient at the top of the pore ($x = 0$) is:

$$\left.\frac{\mathrm{d}C}{\mathrm{d}x}\right|_{x=0} = \frac{C_0}{C^*}\cdot\frac{\kappa}{l}\cdot\tanh(\kappa). \tag{10}$$

Outside the pore, the oxygen concentration gradient from the electrolyte is given by a Koutecky–Levich type equation [24]:

$$\left.\frac{\mathrm{d}\hat{C}}{\mathrm{d}x}\right|_{x=0} = \frac{C^* - \hat{C}_0}{\delta_{O_2}}, \tag{11}$$

where $\delta_{O_2} = 1.612\cdot\omega^{-\frac{1}{2}}\cdot\nu^{\frac{1}{6}}\cdot D^{\frac{1}{3}}$ is the convective–diffusion layer thickness and $\hat{C}$ represents the O_2 concentration outside the pore.

The O_2 concentration is a continuous function $\left(\hat{C}_0 = C_0\right)$ and the flux incoming the pores equals the flux at the electrolyte interface. However, since the electrode has many pores of different length and radius, it was assumed that the O_2 concentration to be the same on the top of all pores and that incoming O_2 flux from the electrolyte must equal the sum of all pore fluxes (equation (12)).

$$A_{\mathrm{geo}}\cdot D\cdot\left.\frac{\mathrm{d}\hat{c}}{\mathrm{d}z}\right|_{x=0} = \sum_{\substack{\mathrm{all}\\ \mathrm{pores}}}\pi\cdot r^2\cdot D\cdot\left.\frac{\mathrm{d}c}{\mathrm{d}z}\right|_{z=0}. \tag{12}$$

By combining equations (10)–(12) we obtain the Koutecky–Levich type equation for the thin porous layer RDE (see derivation in SI):

$$\frac{1}{i} = \frac{1}{n_{e^-}\cdot F\cdot C^*_{O_2}\cdot k\cdot\sum A_{p_i}\frac{\tanh\kappa_i}{\kappa_i}} + \frac{1}{0,62F\cdot A_{\mathrm{geo}}n_e C^*_0 D^{2/3}\nu^{-\frac{1}{6}}\omega^{-\frac{1}{2}}}. \tag{13}$$

With $A_{p_i} = \sum 2\cdot\pi\cdot r\cdot l$ being the electroactive area corresponding to pores with the same κ_i.

The difference with Koutecky–Levich equation for a flat RDE, relies on the kinetic current, i_k. Our model indicates that the porous properties of the electrode affect i_k due to the factor $\sum A_{p_i}\frac{\tanh\kappa_i}{\kappa_i}$, which resembles de Levie's admittance modulating factor. The porous structure contribution is included in the dimensionless quantity $\kappa^2 = k\cdot\left(\frac{rD}{2l^2}\right)^{-1}$, which represents the combined diffusion and kinetics within the pores. When all pores have low κ, ($\tanh\kappa\to\kappa$) the modulating factor equals the total electrode active area A_p (see equation (14)), indicating that at low overpotential or for wide and short pores, the oxygen reduction takes place at the thin-film total electroactive area with little oxygen depletion. This explains the linear plot shown in figure 6(A) and allows to obtain the specific activity of the catalyst in the potential range where the approximation is valid by normalizing by total electroactive area.

$$\begin{aligned} i_k|_{\mathrm{low-overpotential}} &\approx n_{e^-}\cdot F\cdot C^*_{O_2}\cdot k\cdot\sum A_{p_i}\\ i_k|_{\mathrm{low-overpotential}} &\approx n_{e^-}\cdot F\cdot C^*_{O_2}\cdot k\cdot A_p \end{aligned}. \tag{14}$$

When all pores have high κ ($\tanh\kappa\to 1$) the convective–diffusion limiting current is reached for large k or large and thin pores, i.e. the oxygen concentration is depleted at the top of the pores. In this case,

$$i_k|_{\mathrm{high-overpotential}} \approx n_{e^-}\cdot F\cdot C^*_{O_2}\cdot k\cdot\sum\frac{A_{p_i}}{\kappa_i} \tag{15}$$

$i_k|_{\mathrm{high-overpotential}}$ can be expressed in terms of parameters obtained from impedance analysis as:

$$i_k|_{\mathrm{high-overpotential}} \approx n_{e^-}\cdot F\cdot C^*\cdot\sqrt{2C_{dl}\cdot\rho\cdot D\cdot k}\cdot A_p\cdot\overline{\alpha_0} \tag{16}$$

due to the relation:

$$\frac{1}{2\rho\cdot C_{dl}\alpha_0^2} = \frac{2l^2}{r}. \tag{17}$$

It should be noticed that when the oxygen consumption is larger than its diffusion within the pores only the top of the film is reducing O_2, and this region gets smaller the larger κ (exponential decrease). As a result, the total kinetic current i_k increases according to $\sqrt{k}$ and not to k, i.e. Tafel slope at HO should be half of the slope at low-overpotentials (LO). Equation (16) explains the trend of $i_k|_{\mathrm{high-overpotential}}$ with $A_p\cdot\overline{\alpha_0}$ seen in figure 6(B).

Figure 7 shows normalized kinetic currents ($i_{k,\mathrm{norm}}$) by total electroactive area of the same experiments shown in figure 5. The curves overlap at LO because all electrodes were prepared using the same catalyst, i.e. have the same specific activity, and separate (shift) at higher potentials according to their $\overline{\alpha_0}$, as predicted by equation (16). On the other hand, the normalized kinetic current increases with $\overline{\alpha_0}$. Ke *et al* [25] observed the same behavior when comparing porous platinum electrodes with increasing amount of deposited catalyst on the disc. The LO approximation is valid for $\kappa\leqslant 0.2$ and the maximum value of $i_{k,\mathrm{norm}}$ where all particles in the film are active for the ORR is proportional to ${\alpha_0}^2$ (equation (18)), i.e. according to the model

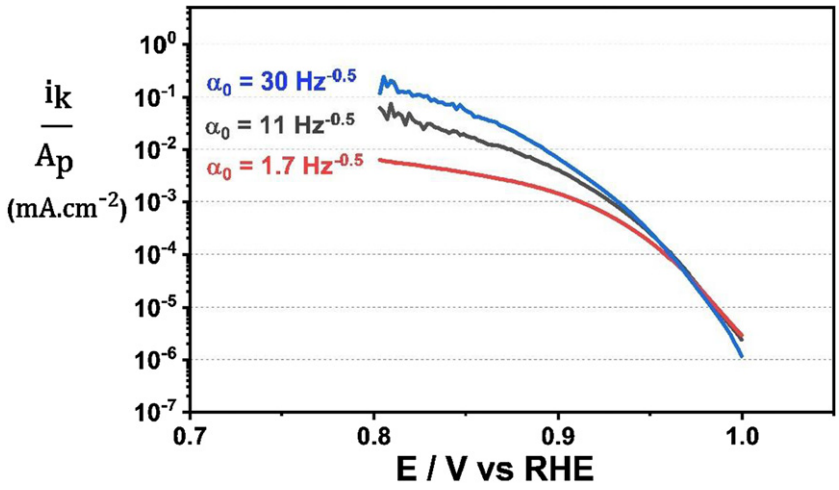

Figure 7. Normalized kinetic current ($i_{k,\mathrm{norm}}$) of the three RT-FePc electrodes shown in figure 5.

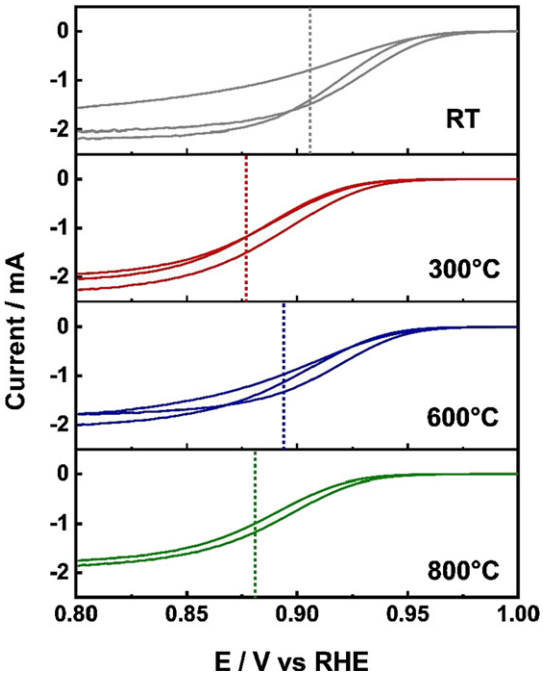

Figure 8. RDE measurements of all catalyst. Dotted line represents average $E_{\text{half-wave}}$.

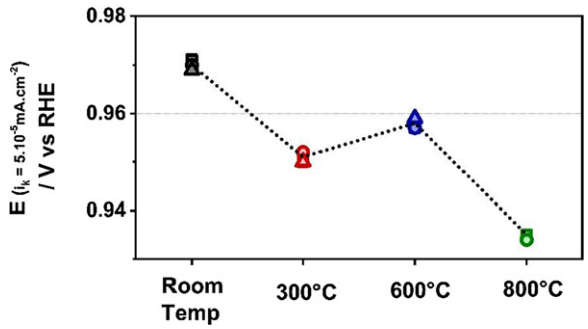

Figure 9. Potential at normalized kinetic current of 5×10^{-5} mA cm^{-2} as a function of heat treatment temperature. The electroactive area correction was based on an assumed specific capacity of 2 μF cm^{-2}.

higher $i_{k,\mathrm{norm}}$ are predicted the higher $\overline{\alpha_0}$.

$$\kappa^2 = \frac{k}{\frac{rD}{2l^2}} \leqslant 0.04$$

$$\kappa^2 = \frac{-nFC^*k}{-nFC^*\frac{rD}{2l^2}} \leqslant 0.04 \qquad (18)$$

$$i_{k,\mathrm{norm}} \leqslant 0.04 \cdot -n \cdot F \cdot D \cdot C^* \cdot 2\rho \cdot C_{\mathrm{dl}}{\alpha_0}^2$$

The model does not account for the experimental data at HO as well as it does at LO, as shown in figures 6(A) and (B). Therefore, a better definition of the specific catalytic activity from $i_{k,\mathrm{norm}}$ with the low κ approximation is needed. Since the potential range where the low κ approximation is valid may depend on the catalyst, a characteristic potential for a predefined value $i_{k,\mathrm{norm}}$ is a better indicator of the electrocatalytic activity than a current $i_{k,\mathrm{norm}}$ at a predefined potential.

It is interesting to notice that this limitation can be removed by using electrodes with higher penetration ratios. The potential window where the low κ approximation is valid can include a wider potential range where the RDE current changes if electrodes have large enough $\overline{\alpha_0}$ ($\geqslant$30 Hz$^{-0.5}$ according to the present results).

Figure 8 compares the RDE currents obtained in O_2 saturated 0.1 M KOH (pH = 13) for all catalysts studied. Inspection of the average half wave potential, $E_{\text{Half-wave}}$ (dashed line) shows that the activity decreases after heat treating at 300 °C, rises at 600 °C and decreases again at 800 °C to the same value observed for FePc-300 °C. Lalande [39] observed that non-pyrolyzed FePc/C catalyst had the lowest activity but the same trend for the other catalysts. We have confirmed that FePc-RT exhibits poor ORR activity if tested before cycling because few FePc molecules are electrically connected to the carbon support. After few oxidation–reduction cycles, the redox charge rises and the electro catalytic activity improves significantly. Note that Komba *et al* [40] obtained an excellent FePc based catalyst for ORR without using any heat treatment in its preparation in agreement with our result.

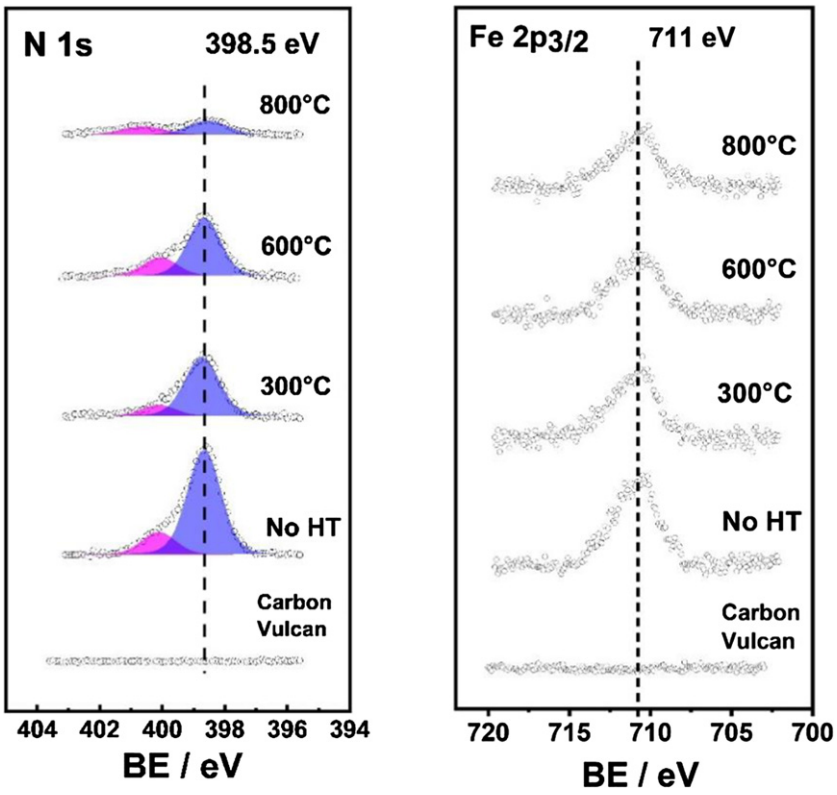

Figure 10. N 1s and Fe $2p_{3/2}$ XPS spectra of carbon Vulcan particles and synthetized materials.

Figure 9 shows the specific activity as a function of the heat treatment temperature for the electrodes described in figure 8. The dispersion observed in figure 8 was reduced significantly after normalizing, and the activity trend changed since the specific activity corresponding to FePc-800 °C was smaller than FePc-300 °C. Both catalysts showed similar activity in RDE experiments (figure 8) due to the much higher specific area of FePc-800 °C (see figure 3-bottom panel).

The catalytic activity improvement for FePc-600 °C as compared to FePc-300 °C was kept after normalization which is consistent with results reported elsewhere [39, 41, 42]. This improvement has been widely discussed but still there is no agreement in the literature. Among the possibilities it has been suggested better dispersion of the supported chelate, the formation of a non-identified Fe–N active site [15] and a modification in the electronic structure of the central metal due to a reaction of the chelate and the carbon support surface [42, 43].

In order to gain information on the catalysts Fe and N surface composition in the present work, we have combined XPS with electrochemical estimation of the redox sites concentration on the surface.

Figure 10 shows the N 1s and Fe $2p_{3/2}$ XPS spectra corresponding to carbon Vulcan support and the FePc-RT, FePc-300, FePc-600 and FePc-800 catalysts. The N 1s XPS signal of FePc-RT is composed of two main contributions. The most intense is centered at 398.5 eV and is due to the N atoms in the FePc molecule [44], while the second is centered at 400.2 eV and may be due to amine groups [45]. Although the secondary contribution is not expected since all nitrogen are equivalent in FePc, it has also been observed by other authors [39, 46, 47]

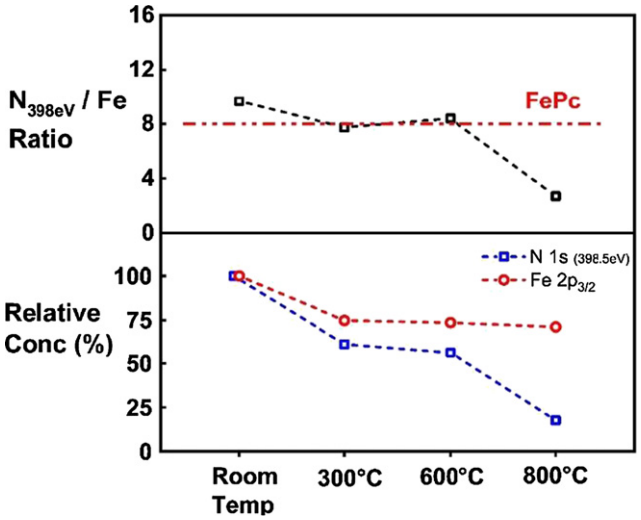

Figure 11. Top panel: ratio between integrated intensities of N 1s(298.5 eV) and Fe $2p_{3/2}$ signals corrected by the corresponding sensitivity factors. Dotted line corresponds to ratio expected for FePc. Bottom panel: intensities of N 1s(298.5 eV) and Fe $2p_{3/2}$ relative to the not heat-treated material.

and is probably due to the co-adsorption of unwanted species during catalyst preparation. Although the intensity of the Fe $2p_{3/2}$ signal changes with temperature the binding energy position remains constant suggesting that the iron oxidation state distribution of remains similar to that in the non-pyrolyzed material.

Figure 12(A) shows that the ratio between the N 1s signal at 398.5 eV and the Fe $2p_{3/2}$ signal (corrected by the

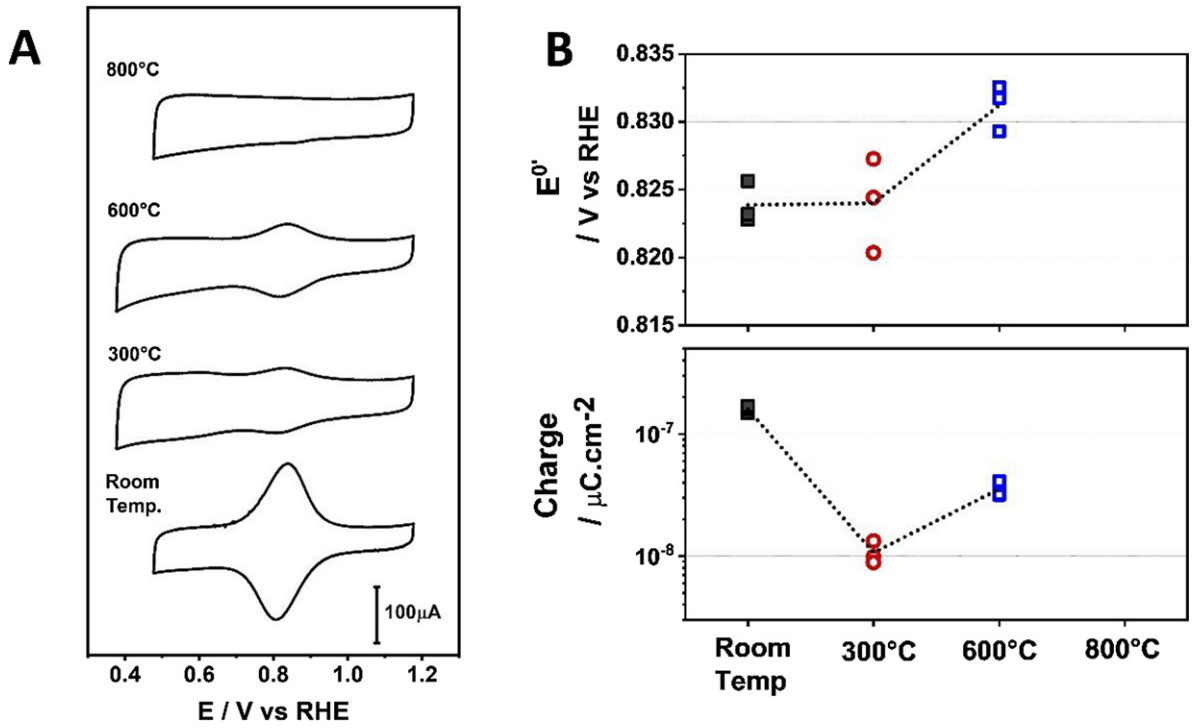

Figure 12. (A) Cyclic voltammetry example for every material studied. (B) Top panel: standard potential of the electron transfer process ($E^{0\prime}$) as a function of heat treatment temperature. Bottom panel: charge of FePc redox couple normalized by electroactive area (obtained from impedance fitting) as a function of heat treatment temperature.

corresponding sensitivity factors) from 300 °C to 600 °C is roughly 8:1 in agreement with the molecular stoichiometry. Thus, the observed decrease in the N 1s and Fe $2p_{3/2}$ intensities in this temperature range is probably due to desorption of intact FePc molecules. This is consistent with previous work [39, 48, 49] which has shown that Fe–N_4 moieties do not suffer thermal decomposition at pyrolysis temperatures below 600 °C.

Annealing from 600 °C to 800 °C causes a further decrease in the N signal at 398.5 eV, while the Fe $2p_{3/2}$ signal remains almost constant. Consequently, the ratio N(298.5 eV)/Fe decreases to almost 3, indicating the molecular stoichiometry is lost. On the other hand, the binding energy of the Fe $2p_{3/2}$ signal remains unmodified thus suggesting that the iron oxidation state is similar to that of the FePc molecule. Then, it is concluded that Fe–N_4 moieties are decomposed upon heat treatment at 800 °C and nitrogen containing products are desorbed while oxidized iron remains at the surface.

The Fe(II)/Fe(III) electrochemical process has been studied with cyclic voltammetry (figure 12(A)), and the corresponding analysis is shown in figure 12(B). The top panel in figure 12(B) reveals that the standard potential of the electron transfer process ($E^{0\prime}$) shifts to slightly higher values for FePc-600 °C, which may be interpreted as change in the chemical environment of the metal center [42, 50, 51]. On the other hand, the bottom panel shows that the integrated charge of the FePc peaks is highest in FePc-RT, with a ten-fold decrease after 300 °C heat treatment, surprisingly, increases slightly for FePc-600 °C but no peak has been observed for FePc-800 °C, which is consistent with destruction of Fe–N_4 moieties as found from XPS.

Table 1. Surface concentration of FePc relative to FePc-RT obtained by XPS and cyclic voltammetry.

	XPS	CV peak
FePc-RT	1	1
FePc-300 °C	0.62	0.07
FePc-600 °C	0.56	0.22

Table 1 compares the surface concentration of FePc relative to FePc-RT obtained by XPS and integration of voltammetry redox peaks. XPS analysis shows very similar Fe–N_4 surface concentration for FePc-300 °C and FePc-600 °C and that is some 60% lower than in FePc-RT. The relative redox charge is much lower for both catalyst. Hence, heat treatment not only reduced the concentration but also silenced the electrochemical activity of a fraction of the surface molecules. The fact that there were more electroactive redox species at 600 °C than at 300 °C may be due to a better rearrangement of the molecules at higher temperature in the thermal treatment.

The main purpose of the comparative analysis carried out in this work has been to find strong correlations between surface composition and activity in order to elucidate the nature of the electro catalytic sites. Figure 13 shows a linear correlation between the specific activity and the logarithm of Fe–N_4 surface concentration obtained from the electroactive charge. It has been proposed that the activity increases after heat treatment at 600 °C due to the formation of a new active site, which would be more active than the original FePc. However, our

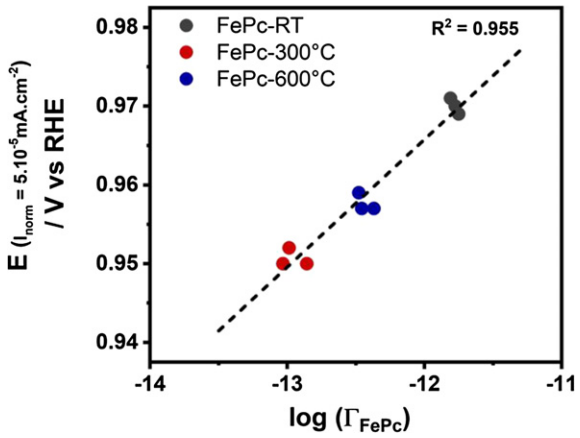

Figure 13. Potential at which normalized kinetic current is 5×10^{-5} mA cm^{-2} as a function of the logarithm of specific FePc surface concentration calculated by integration of CV.

results indicate that the activity in basic media increases due to a change in the surface concentration of electroactive Fe–N_4 moieties. This illustrates one of the biggest problems when using XPS to find the active site in complex catalysts. While FePc-300 °C and FePc-600 °C show the same XPS FePc surface concentration, the redox charge from cyclic voltammetry determines the concentration of the electroactive sites for the ORR.

4. Conclusions

By combining RDE, linear scan voltammetry and electrochemical impedance spectroscopy for thin porous RDE electrodes, we could separate the effects on the activity. of electroactive area, O_2 penetrability and chemical surface composition.

Normalization of RDE kinetic currents by the electroactive area at low overpotential has been applied to heat-treated FePc electrocatalyst dispersed on carbon. Comparison of the XPS surface composition and the redox charge has shown Fe and N present on all surfaces. The N:Fe ratio of FePc (8:1) was conserved up to 600 °C but decreases at 800 °C while FePc active sites are lost.

A very good correlation has been found between the ORR electro catalytic activity and the surface concentration of FePc electroactive of sites after normalizing by the electroactive area. This result suggests that the activity per FeN_4 active site is the same in these catalysts.

Acknowledgments

Funding from ANPCyT Grant PICT-2016-4380 is greatly appreciated. EJC and FJW are reseach fellows of CONICET and Professors of Universidad de Buenos Aires, FGD acknowledges a joint doctoral scholarship from CONICET and Y-TEC and CF acknowledges a doctoral scholarship from CONICET.

Data availability statement

All data that support the findings of this study are included within the article (and any supplementary files).

ORCID iDs

Federico Gabriel Davia https://orcid.org/0000-0002-6194-2734
Ernesto Julio Calvo https://orcid.org/0000-0003-0397-2406

References

[1] Bockris J 2008 Hydrogen no longer a high cost solution to global warming: new ideas *Int. J. Hydrog. Energy* **33** 2129–31
[2] Bashyam R and Zelenay P 2006 A class of non-precious metal composite catalysts for fuel cells *Nature* **443** 63–6
[3] Wu G, More K L, Johnston C M and Zelenay P 2011 High-performance electrocatalysts for oxygen reduction derived from polyaniline, iron, and cobalt *Science* **332** 443
[4] Proietti E, Jaouen F, Lefèvre M, Larouche N, Tian J, Herranz J and Dodelet J-P 2011 Iron-based cathode catalyst with enhanced power density in polymer electrolyte membrane fuel cells *Nat. Commun.* **2** 416
[5] Kisand K, Sarapuu A, Peikolainen A-L, Seemen H, Kook M, Käärik M, Leis J, Sammelselg V and Tammeveski K 2018 Oxygen reduction on Fe- and Co-containing nitrogen-doped nanocarbons *ChemElectroChem* **5** 2002–9
[6] Osmieri L 2019 Transition metal–nitrogen–carbon (M–N–C) catalysts for oxygen reduction reaction. Insights on synthesis and performance in polymer electrolyte fuel cells *ChemEngineering* **3** 16
[7] Van Pham C, Klingele M, Britton B, Vuyyuru K R, Unmuessig T, Holdcroft S, Fischer A and Thiele S 2017 Tridoped reduced graphene oxide as a metal-free catalyst for oxygen reduction reaction demonstrated in acidic and alkaline polymer electrolyte fuel cells *Adv. Sustain. Syst.* **1** 1600038
[8] Wu Y-J *et al* 2018 Three-dimensional networks of S-doped Fe/N/C with hierarchical porosity for efficient oxygen reduction in polymer electrolyte membrane fuel cells *ACS Appl. Mater. Interfaces* **10** 14602–13
[9] Lefèvre M, Proietti E, Jaouen F and Dodelet J-P 2009 Iron-based catalysts with improved oxygen reduction activity in polymer electrolyte fuel cells *Science* **324** 71–4
[10] Wu G *et al* 2011 Synthesis-structure-performance correlation for polyaniline–Me–C non-precious metal cathode catalysts for oxygen reduction in fuel cells *J. Mater. Chem.* **21** 11392–405
[11] Kneebone J L *et al* 2017 A combined probe-molecule, Mössbauer, nuclear resonance vibrational spectroscopy, and density functional theory approach for evaluation of potential iron active sites in an oxygen reduction reaction catalyst *J. Phys. Chem* C **121** 16283–90
[12] Ferrandon M, Kropf A J, Myers D J, Artyushkova K, Kramm U, Bogdanoff P, Wu G, Johnston C M and Zelenay P 2012 Multitechnique characterization of a polyaniline–iron–carbon oxygen reduction catalyst *J. Phys. Chem* C **116** 16001–13
[13] Kramm U I, Lefèvre M, Larouche N, Schmeisser D and Dodelet J P 2014 Correlations between mass activity and physicochemical properties of Fe/N/C catalysts for the ORR in PEM fuel cell via 57Fe Mössbauer spectroscopy and other techniques *J. Am. Chem. Soc.* **136** 978–85
[14] Maldonado S and Stevenson K J 2004 Direct preparation of carbon nanofiber electrodes via pyrolysis of iron(II) phthalocya-

nine: electrocatalytic aspects for oxygen reduction *J. Phys. Chem* B **108** 11375–83
[15] Scherson D, Tanaka A A, Gupta S L, Tryk D, Fierro C, Holze R, Yeager E B and Lattimer R P 1986 Transition metal macrocycles supported on high area carbon: pyrolysis-mass spectrometry studies *Electrochim. Acta* **31** 1247–58
[16] Xu Y, Dzara M J, Kabir S, Pylypenko S, Neyerlin K and Zakutayev A 2020 X-ray photoelectron spectroscopy and rotating disk electrode measurements of smooth sputtered Fe–N–C films *Appl. Surf. Sci.* **515** 146012
[17] Chung H T, Cullen D A, Higgins D, Sneed B T, Holby E F, More K L and Zelenay P 2017 Direct atomic-level insight into the active sites of a high-performance PGM-free ORR catalyst *Science* **357** 479
[18] Lefèvre M, Dodelet J P and Bertrand P 2002 Molecular oxygen reduction in PEM fuel cells: evidence for the simultaneous presence of two active sites in Fe-based catalysts *J. Phys. Chem* B **106** 8705–13
[19] Holby E F and Zelenay P 2016 Linking structure to function: the search for active sites in non-platinum group metal oxygen reduction reaction catalysts *Nano Energy* **29** 54–64
[20] Artyushkova K, Serov A, Rojas-Carbonell S and Atanassov P 2015 Chemistry of multitudinous active sites for oxygen reduction reaction in transition metal–nitrogen–carbon electrocatalysts *J. Phys. Chem* C **119** 25917–28
[21] Jia Q *et al* 2016 Spectroscopic insights into the nature of active sites in iron–nitrogen–carbon electrocatalysts for oxygen reduction in acid and the redox mechanisms *Nano Energy* **29** 65–82
[22] Jia Q *et al* 2015 Experimental observation of redox-induced Fe–N switching behavior as a determinant role for oxygen reduction activity *ACS Nano* **9** 12496–505
[23] von Kármán T 1921 Über laminare und turbulente Reibung *Z. Angew. Math. Mech.* **1** 233–52
[24] Bard A J and Faulkner L R 2000 *Electrochemical Methods: Fundamentals and Applications* 2nd edn (New York: Wiley)
[25] Ke K, Hiroshima K, Kamitaka Y, Hatanaka T and Morimoto Y 2012 An accurate evaluation for the activity of nano-sized electrocatalysts by a thin-film rotating disk electrode: oxygen reduction on Pt/C *Electrochim. Acta* **72** 120–8
[26] Garsany Y, Baturina O A, Swider-Lyons K E and Kocha S S 2010 Experimental methods for quantifying the activity of platinum electrocatalysts for the oxygen reduction reaction *Anal. Chem.* **82** 6321–8
[27] Kocha S S *et al* 2017 Best practices and testing protocols for benchmarking ORR activities of fuel cell electrocatalysts using rotating disk electrode *Electrocatalysis* **8** 366–74
[28] Srinivasan S, Hurwitz H D and Bockris J O M 1967 Fundamental equations of electrochemical kinetics at porous gas-diffusion electrodes *J. Chem. Phys.* **46** 3108–22
[29] Masa J, Batchelor-McAuley C, Schuhmann W and Compton R G 2014 Koutecky–Levich analysis applied to nanoparticle modified rotating disk electrodes: electrocatalysis or misinterpretation *Nano Res.* **7** 71–8
[30] Perez J, Gonzalez E R and Ticianelli E A 1998 Oxygen electrocatalysis on thin porous coating rotating platinum electrodes *Electrochim. Acta* **44** 1329–39
[31] De Levie R 1967 Electrochemical response of porous and rough electrodes *Adv. Electrochem. Electrochem. Eng.* **6** 329–97
[32] de Levie R 1963 On porous electrodes in electrolyte solutions *Electrochim. Acta* **8** 751–80
[33] Newman J and Tiedemann W 1975 Porous-electrode theory with battery applications *AIChE J.* **21** 25–41
[34] Meyers J P, Doyle M, Darling R M and Newman J 2000 The impedance response of a porous electrode composed of intercalation particles *J. Electrochem. Soc.* **147** 2930
[35] Lasia A 2009 Modeling of impedance of porous electrodes *Modern Aspects of Electrochemistry* vol 43 Berlin: Springer pp 67–137
[36] Song H-K, Jung Y-H, Lee K-H and Dao L H 1999 Electrochemical impedance spectroscopy of porous electrodes: the effect of pore size distribution *Electrochim. Acta* **44** 3513–9
[37] Jaouen F *et al* 2009 Cross-laboratory experimental study of non-noble-metal electrocatalysts for the oxygen reduction reaction *ACS Appl. Mater. Interfaces* **1** 1623–39
[38] Charreteur F, Jaouen F, Ruggeri S and Dodelet J-P 2008 Fe/N/C non-precious catalysts for PEM fuel cells: influence of the structural parameters of pristine commercial carbon blacks on their activity for oxygen reduction *Electrochim. Acta* **53** 2925–38
[39] Lalande G, Faubert G, Côté R, Guay D, Dodelet J P, Weng L T and Bertrand P 1996 Catalytic activity and stability of heat-treated iron phthalocyanines for the electroreduction of oxygen in polymer electrolyte fuel cells *J. Power Sources* **61** 227–37
[40] Komba N, Zhang G, Wei Q, Yang X, Prakash J, Chenitz R, Rosei F and Sun S 2019 Iron (II) phthalocyanine/N-doped graphene: a highly efficient non-precious metal catalyst for oxygen reduction *Int. J. Hydrog. Energy* **44** 18103–14
[41] Miller H A *et al* 2016 Heat treated carbon supported iron(ii)phthalocyanine oxygen reduction catalysts: elucidation of the structure-activity relationship using x-ray absorption spectroscopy *Phys. Chem. Chem. Phys.* **18** 33142–51
[42] van Veen J A R, Colijn H A and van Baar J F 1988 On the effect of a heat treatment on the structure of carbon-supported metalloporphyrins and phthalocyanines *Electrochim. Acta* **33** 801–4
[43] van Veen J A R, van Baar J F and Kroese K J 1981 Effect of heat treatment on the performance of carbon-supported transition-metal chelates in the electrochemical reduction of oxygen *J. Chem. Soc., Faraday Trans. 1* **77** 2827–43
[44] Isvoranu C, Åhlund J, Wang B, Ataman E, Mårtensson N, Puglia C, Andersen J N, Bocquet M-L and Schnadt J 2009 Electron spectroscopy study of the initial stages of iron phthalocyanine growth on highly oriented pyrolytic graphite *J. Chem. Phys.* **131** 214709
[45] Tagliazucchi M, Williams F J and Calvo E J 2007 Effect of acid−base equilibria on the Donnan potential of layer-by-layer redox polyelectrolyte multilayers *J. Phys. Chem* B **111** 8105–13
[46] Lalande G, Côté R, Tamizhmani G, Guay D, Dodelet J P, Dignard-Bailey L, Weng L T and Bertrand P 1995 Physical, chemical and electrochemical characterization of heat-treated tetracarboxylic cobalt phthalocyanine adsorbed on carbon black as electrocatalyst for oxygen reduction in polymer electrolyte fuel cells *Electrochim. Acta* **40** 2635–46
[47] Ladouceur M, Lalande G, Guay D, Dodelet J P, Dignard-Bailey L, Trudeau M L and Schulz R 1993 Pyrolyzed cobalt phthalocyanine as electrocatalyst for oxygen reduction *J. Electrochem. Soc.* **140** 1974–81
[48] Gunasekara I, Ates M N, Mukerjee S, Plichta E J, Hendrickson M A and Abraham K M 2017 Solid phase FePC catalysts for increased stability of oxygen reduction reaction intermediates at the cathode/electrolyte interface in lithium air batteries *J. Electrochem. Soc.* **164** A760–9
[49] Bambagioni V *et al* 2011 Single-site and nanosized Fe–Co electrocatalysts for oxygen reduction: synthesis, characterization and catalytic performance *J. Power Sources* **196** 2519–29
[50] Zagal J H, Ponce I, Báez D, Venegas R, Pavez J, Páez M and Gulppi M 2012 A possible interpretation for the high catalytic activity of heat-treated non-precious metal Nx/C catalysts for O_2 reduction in terms of their formal potentials *Electrochem. Solid-State Lett.* **15** B90
[51] Tylus U, Jia Q, Strickland K, Ramaswamy N, Serov A, Atanassov P and Mukerjee S 2014 Elucidating oxygen reduction active sites in pyrolyzed metal–nitrogen coordinated non-precious-metal electrocatalyst systems *J. Phys. Chem* C **118** 8999–9008